Received: 17 August 2024 | Revised: 28 December 2024 | Accepted: 30 December 2024

DOI: 10.1002/mp.17638

RESEARCH ARTICLE

MEDICAL PHYSICS

Scanning K-edge subtraction (SKES) imaging with laser-compton x-ray sources

Trevor Reutershan[1,2] | **Christine V. Nguyen**[1] | **Haytham H. Effarah**[1,2] | **Eric C. Nelson**[1] | **Kyle D. Chesnut**[1] | **Christopher P. J. Barty**[1,2,3]

[1]Department of Physics and Astronomy, University of California - Irvine, Irvine, California, USA

[2]Beckman Laser Institute and Medical Clinic, University of California - Irvine, Irvine, California, USA

[3]Lumitron Technologies, Inc, Irvine, California, USA

Correspondence
Trevor Reutershan, Department of Physics and Astronomy, University of California - Irvine, Irvine, California 92697, USA.
Email: treuters@hs.uci.edu

Funding information
National Institutes of Health, Grant/Award Number: T32GM008620

Abstract

Background: K-edge subtraction (KES) imaging is a dual-energy imaging technique that enhances contrast by subtracting images taken with x-rays that are above and below the K-edge energy of a specified contrast agent. The resulting reconstruction spatially identifies where the contrast agent accumulates, even when obscured by complex and heterogeneous distributions of human tissue. This method is most successful when x-ray sources are quasimonoenergetic and tunable, conditions that have traditionally only been met at synchrotrons. Laser-Compton x-ray sources (LCSs) are a compact alternative to synchrotron radiation with a quasimonoenergetic x-ray spectrum. One limitation in the clinical application of KES imaging with LCSs has been the extensive time required to tune the x-ray spectrum to two different energies.

Purpose: We introduce an imaging technique called scanning K-edge subtraction (SKES) that leverages the angle-correlated laser-Compton x-ray spectrum in the setting of mammography. The feasibility and utility of this technique will be evaluated through a series of simulation studies. The goal of SKES imaging is to enable rapid K-edge subtraction imaging using a laser-Compton x-ray source. The technique does not rely on the time-consuming process of tuning laser-Compton interaction parameters.

Methods: Laser-Compton interaction physics are modeled using conditions based on an X-band linear electron accelerator architecture currently under development using a combination of 3D particle tracking software and Mathematica. The resulting angle-correlated laser-Compton x-ray beam is propagated through digitally compressed breast phantoms containing iodine contrast-enhanced inserts and then to a digital flat-panel detector using a Matlab Monte Carlo propagation software. This scanning acquisition technique is compared to the direct energy tuning method (DET), as well as to a clinically available dual-energy contrast-enhanced mammography (CEM) system.

Results: KES imaging in a scanning configuration using an LCS was able to generate a KES image of comparable quality to the direct energy tuning method. SKES was able to detect tumors with iodine contrast concentrations lower than what is clinically available today including lesions that are typically obscured by dense fibroglandular tissue. After normalizing to mean glandular dose, SKES is able to generate a KES image with equal contrast to CEM using only 3% of the dose.

Conclusions: By leveraging the unique quasimonochromatic and angle-correlated x-ray spectrum offered by LCSs, a contrast-enhanced subtraction image can be obtained with significantly more contrast and less dose compared to conventional systems, and improve tumor detection in patients with dense breast tissue. The scanning configuration of this technique could accelerate the clinical translation of this technology.

KEYWORDS
contrast-enhanced mammography, dual-energy, K-edge subtraction, laser-Compton

1 | INTRODUCTION

K-edge subtraction (KES) imaging is a dual-energy x-ray modality that images the accumulation of contrast agents, typically iodine-based. KES takes advantage of the discontinuous change in the photoabsorption cross-section of the inner K-shell electrons at a characteristic energy that is unique to each element referred to as the K-edge. For iodine, the K-edge energy is 33.169 keV (see Figure 1a). By taking two images, one with energy tuned just above the K-edge and another with energy tuned just below the K-edge, subtraction of these two images ideally leaves enhancement at the place of contrast uptake only. Since tumor angiogenesis tends to result in leaky vasculature, KES has been used in the past for cancer imaging. This paper will evaluate a recently proposed method of KES imaging using a unique, compact, tunable, quasimonoenergetic class of x-ray sources known as laser-Compton sources (LCSs).[1] Because the most clinically used application of KES is in dual-energy mammographic cancer screening, known as contrast-enhanced mammography (CEM),[2] the authors will evaluate this method in the setting of mammography.

1.1 | Dual-energy imaging and mammography

Breast cancer is the most diagnosed cancer and the second cause of cancer death in women in the United States.[3] Breast cancer outcomes have been improving since the implementation of widespread mammographic screening.[4] Despite the success of mammography, there are still many improvements that need to be made. Mammographic screening can miss up to 20% of cancers[5,6] and can have a positive predictive value below 5% in certain situations.[7] For the patient population with a high fraction of fibroglandular tissue, the diagnostic power of mammograms is significantly worse and can miss as much as up to 70% of breast cancers in that population.[5,6] This fact led the US Food & Drug Administration to require disclosure of breast density, and a statement that mammography alone may not be sufficient in patients with dense breast tissue suggesting higher-level imaging to be performed.[8] This highlights a clinical need to improve mammography, especially for the at-risk population, namely those patients with dense breasts.

CEM, also referred to as contrast-enhanced dual-energy mammography, contrast-enhanced digital mammography, contrast-enhanced spectral mammography, or simply dual-energy mammography, has been in clinical use for more than a decade.[9] It has proven to be a useful imaging modality, having better diagnostic power than traditional mammography and a sensitivity to breast cancer that is on par with 3-dimensional contrast-enhanced magnetic resonance imaging (MRI)[10] and even mammography with ultrasound combined.[11] Despite its superior sensitivity to mammography, CEM has not gained widespread clinical traction, likely due to the need for higher-level health professionals, the increased risk of adverse effects because of the use of intravenous iodine-based contrast agents, and the general increase in dose obtained from two separate exposures.

Traditional x-ray tubes are the sources used in dual-energy mammography devices. They produce bremsstrahlung radiation that is broad in bandwidth and are tuned to peak photon energies that are more than 10 keV from the iodine K-edge. Since K-edge photoabsorption is a near-discontinuous physics process, KES would show the greatest enhancement having energies that are as close as possible to the K-edge of the contrast material. In recent history, synchrotrons have been investigated for use in KES imaging since they have the capability to produce narrow energy bandwidth radiation when combined with crystal bandwidth filters, that is ideal for KES.[12] However, these sources are institutional-sized ring electron accelerators and possess no feasible downscale to fit within a clinic. LCSs, on the other hand, are compact and produce synchrotron-like tunable radiation that is narrow in energy bandwidth (BW) making them a viable source for clinical translation of KES imaging.[13,14]

1.2 | Laser-Compton sources

LCSs work by colliding laser light with an accelerated electron beam (see Figure 1b). The two beams undergo

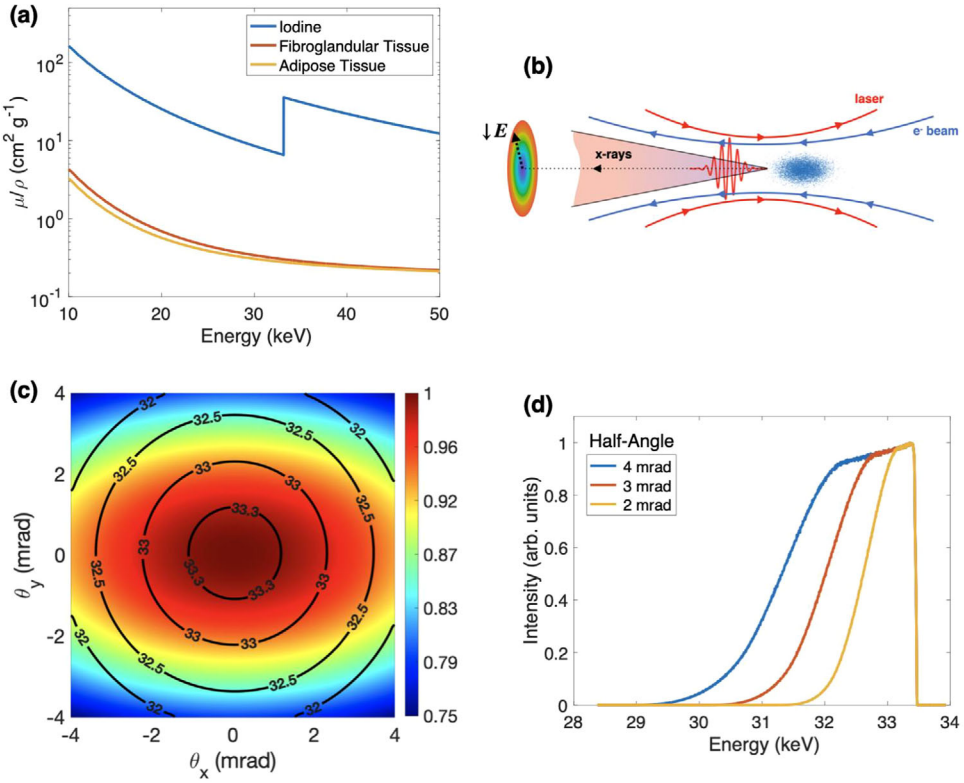

FIGURE 1 (a) Attenuation coefficients of iodine, fibroglandular tissue, and adipose tissue in the energy range used in this study. (b) Diagram of laser-Compton interaction. A well-timed overlap of a laser pulse and an accelerated electron bunch will under Compton scattering to produce x-rays in the direction of electron beam propagation. (c) Laser-Compton intensity heat map with mean energy contours overlay. (d) Integrated laser-Compton energy spectrum over different half-angle collimations. More aggressive collimation blocks low energy photons at larger half-angles resulting in decreasing energy bandwidth, but also causes lower overall flux.

Compton scattering and the energy of the scattered radiation is double Doppler upshifted in the laboratory frame into the x-ray regime. The energy of the scattered radiation, E_C, can be derived from relativistic energy-momentum conservation.[13] For a head-on collision and small scattering angles, the scattered radiation at angle θ has an energy that approaches the functional form[15]

$$E_C(\theta) = \frac{4\gamma^2 E_L}{1 + \gamma^2\theta^2 + 4\gamma k_0 \lambda\!\!\!^{-}_c},$$

where γ is the electron beam's Lorentz factor $\gamma = E_e/m_e c^2 + 1$, with E_e being the kinetic energy of the electron and m_e the rest mass of the electron, E_L is the energy of the laser photon, k_0 is the wavenumber of the laser photon, and $\lambda\!\!\!^{-}_c$ is the reduced Compton wavelength. The numerator in the energy expression, $4\gamma^2 E_L$, represents the double Doppler upshift that is characteristic of LCSs. Depending on the energy of the electron beam, this results in taking an initial laser photon of energy on the order of a couple of electronvolts to create a scattered photon up to 10's of keV or even MeV energies. By adjusting the energy of the electron beam, the scattered x-rays can be tuned to the desired energy.

The properties of an LCS are dependent on the physical characteristics of both the electron beam and the laser used in the interaction. Mathematically, the spectrum differential in energy and solid angle becomes,[16]

$$\frac{dN}{d\Omega dE} = \int \frac{d\sigma}{d\Omega}\,\delta[E - E_C(\theta)]\,c\,(1+\beta_0)\,n_l(x_\mu)\,n_e(x_\mu)\,d^4x_\mu.$$

Here, N is the number of photons scattered in the solid angle Ω with energy E, $d\sigma/d\Omega$ is the Klien–Nishina differential cross section, c is the speed of light, β_0 is the net reduced speed (v/c) of the electron, and n_l and n_e are respectively the laser and electron densities parameterized in terms of the electron 4-position x_μ. The result of this LCS physics is an energy-intensity spectrum that is dependent on the scattering angle in space. Figure 1c shows an LCS spectrum obtained using a Gaussian laser beam scattering with an electron beam that is Gaussian in space and time. Because the scattering is a dipole phenomenon, the intensity profile follows a dipole radiation pattern that is projected onto the imaging plane where the laser polarization is along the short axis of the x-ray intensity pattern.

While previous and existing Compton sources have demonstrated energy bandwidths in the 10's of percent, optimized sources can reach 0.1% full width at half maximum (FWHM) $\Delta E/E$. It was recently demonstrated energy bandwidths down to 0.5% root-mean-square (rms) are achievable with a distributed charge laser-Compton architecture.[17] This architecture is assumed for the basis of this study and the KES performance of that existing source will be evaluated. Figure 1d shows the integrated energy spectrum of an LCS and its dependence on aperture size. Due to the quasimonoenergetic and tunable properties of LCSs, they have been a subject of study for KES imaging for some time. Previous experimental studies at the Munich Compact Light Source performed iodine-based experimental LCS KES using an iodine filtering method.[18] Computational studies have also been performed using a direct energy tuning (DET) method by simulating two exposures each at a different tuning of the LCS, one study looking at iodine-based contrast[19] and another looking at gadolinium-based contrast agents.[20] These methods, especially DET, take time to implement changing source parameters. Such changes are not trivial and cause significant delay between exposures leading to potential complications and artifacts in the image.

This paper investigates an alternate method, called scanning KES (SKES), using an LCS requiring only a single parameterization/energy tuning and continuous operation without a time delay to obtain two separate images. This method has been proposed previously[1] and makes use of the angle-correlated spectrum created by an LCS. If an LCS is tuned to have an energy spectrum that contains energies that are surrounding a contrast element's K-edge, then one could scan the beam exposing the object to both energies and computationally reconstruct the KES image. This is performed in the setting of iodine-based contrast-enhanced mammography and comparisons of image quality are made to a clinically available CEM source and the DET method.

2 | METHODS

2.1 | Scanning and direct energy tuning K-edge subtraction protocols

SKES makes use of the energy-angle correlation of an LCS x-ray spectrum. For an electron beam with sufficiently small emittance, the mean energy contours follow radial symmetry and have the highest energy in the on-axis direction of propagation of the x-ray beam[21] (Figure 1c). The intensity pattern depends on the polarization of the laser and follows a dipole scattering pattern that is projected onto the imaging plane.[15,22] The result is an energy spectrum that varies depending on the solid angle in space. Due to the spatial separation of the energies, if the energy of the LCS is tuned to include the K-edge energy of a contrast element, one can separate an LCS x-ray spectrum spatially into two zones, an inner spectrum that has photon energies above the K-edge and another that has photon energies below the K-edge.

Since the LCS spectrum has an effective above and below spectrum in a single energy tuning, translating an object through the beam, or equivalently the beam across the object, would expose the object to both energies without need to change source parameters. Software processing can then digitally segregate each zone for appropriate subtraction following exposure. Since the energy of the x-ray is determined by its location in space, the effective high-energy and low-energy exposure zones can be determined in the beam. Those spatial locations can then be used to reconstruct the effective KES image. A simpler and safer approach to a patient would be to use physical blocks of the beam to separate these zones to reduce unnecessary doses to the patient. These blocks may be achieved by solid material of high atomic number machined to the desired shape or coatings applied to the x-ray output window. This study assumes physical blocks in the shape of a circular annulus to appropriately separate two quasi-monoenergetic zones without energies that cross the K-edge energy of iodine (33.169 keV). Figure 2b shows a rendering of a physical beam block.

Figure 2c,d shows an illustration of the proposed patient machine interface. In this concept, the patient is lying prone on the translation bed with their breasts hanging within a cutout. This orientation is the same that is used in dedicated breast CT,[23,24] breast MRI[25] as well as previous breast imaging studies performed at synchrotrons.[26] The scanning direction was chosen to be along the mediolateral axis in the axial plane as it would minimize unnecessary radiation exposure to the patient in a true clinical scenario. Scanning in the opposite dimension along the anteroposterior axis could potentially lead to an increased dose to the chest wall, thorax, and head assuming the beam is incident from the patient's cranial direction. Scanning in the frontal plane, either mediolaterally or craniocaudally, would add an unnecessary dose to the patient's thorax. Imaging in the sagittal plane and scanning along the craniocaudal axis could be another viable approach, as long as the detector is placed along the patient's median plane so as not to image both breasts along the same axis.

For the DET comparison, the protocol used in a prior LCS dual-energy imaging with iodine contrast paper[19] and another study with gadolinium-based contrast agents[20] was used. The full field of the breast phantom was illuminated at an energy tuning just below the iodine K-edge for a single exposure. The energy of the electron beam was then tuned to create a spectrum that is above the iodine K-edge and another full-field exposure was taken.

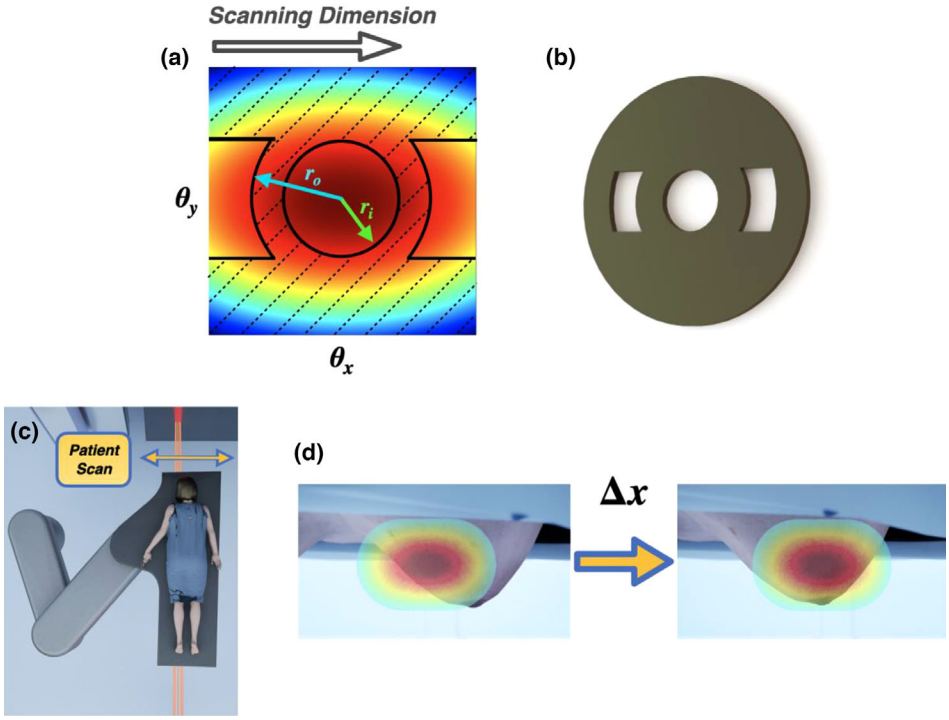

FIGURE 2 (a) Illustration of the SKES configuration. The dashed area represents the blocked regions allowing for separation of energies above and below the K-edge. A 1-dimensional scan will expose the object to both energies allowing for a KES reconstruction. (b) Rendering of a physical beam block machined out of tungsten designed for a circular x-ray beam aperture. (c) Visualization of patient/beam interfacing. (d) Demonstration of scanning via 1-dimensional patient movement through the Compton x-ray beam.

2.2 | x-Ray spectra

The methodology of LCS x-ray spectra, x-ray propagation through material, and image generation was outlined previously[20,27] and will be summarized here. The conventional clinical dual-energy x-ray system chosen to compare to is the commercially available Senographe system with SenoBright protocol by GE Healthcare.[28] SpekPy v2.0.8[29] was used to generate the x-ray spectra from the conventional system. Parameters for the low-energy spectrum are a rhodium target with a 0.025 mm rhodium filter and tube voltage of 29 kVp, whereas a rhodium target with a 0.4 mm copper filter and tube voltage of 45 kVp is used for the high-energy spectrum.

General Particle Tracer (GPT)[30] was used to simulate an accelerated electron beam for the LCS. The acceleration architecture was based on one currently commissioned for the high-flux, distributed-charge, LCS developed at Lumitron Technologies, Inc. in Irvine, California.[17,31,32] The electron beam had an emittance of 0.2 mm mrad and was simulated to the interaction point with the laser, and the resulting phase space was used to calculate the Compton interaction between the two. This calculation was performed in Mathematica using a method that has been described previously.[13,33,34] This method takes the individual macroparticles of the GPT simulation and propagates them through the focus of a Fourier transform limited laser beam that is Gaussian in space and time. The scattered energy-intensity distribution of each macroparticle is then computed and saved. This process is performed for each macroparticle from the GPT simulation and the total spectrum is the sum of the individual macroparticle spectra.[13] A summary of the electron and laser beams used in the laser-Compton interaction has been reported in previous work.[20] The Compton spectra used here had linear polarization and an FWHM BW of 1.1% $\Delta E/E$ for the DET-mode energy tunings.

For the scanning spectra, a circular annulus exclusion area of the spatially-distributed laser-Compton spectrum was defined to make a significant separation between the effective high- and low-energy spectra. A Bayesian optimization method described previously[35] was used to optimize a 6.4% BW laser-Compton spectrum for best contrast-to-noise ratio (CNR) in a test phantom. The test phantom used was the same as in a previous gadolinium study,[20] but with iodine in the place of gadolinium. Figure 2a shows the 2D Compton intensity profile with the relative exclusion zone. The best result after 300 iterations was with r_i = 1 mrad and r_o = 3 mrad. Other shapes of exclusion zones (e.g. elliptical, rectangular, scanning domain, etc…) have been investigated by the authors, and it was discovered an

elliptical annulus may be best overall, but generally it is dependent on the imaging scenario and implementation capabilities of the source and the facility. Such a discussion is beyond the scope of this paper and will be the subject of a future study.

To maintain source parameters that are used clinically, the photon flux and fluence used in contrast-enhanced mammography need to be known, though these values are not readily obtained from the literature. However, these values can be determined from reported experimentally measured air kerma of CEM systems and the known reported exposure times. Using reported air kermas of prior dual-energy studies,[36,37] the source fluence can be estimated and a value of 4.18×10^9 ph cm^{-2} was used for all imaging simulations performed in this study. The exposure time for the low-energy image in CEM is reported to be on the order of 1 s.[11] Using this and the reported air kerma values, this works out to a flux of 1.55×10^{11} ph s^{-1} for the low-energy tuning and 4.06×10^{10} ph s^{-1} for the high-energy tuning of a clinical CEM system, with the exposure time for the high-energy tuning to be longer to accommodate for the lower flux. These flux values are used for the simulations involving the CEM source.

2.3 | x-Ray propagation and image generation

The resulting incident scattered photon spectrum was fed into an in-house x-ray propagation code written in Matlab. The physical processes modeled included photoelectric absorption, coherent scattering, incoherent scattering, and pair production. This code has been verified against Geant4 to be within 0.1% of signal accuracy and is 27,000× faster making multiple large-particle-count simulations computationally feasible.[20] The x-ray propagation software includes the capability of simulating detector noise by including user-defined inputs for the dark, readout, and quantum noises either in units of digital numbers (DNs) per electron or the empirical unit DN per incoming photon. The detector noise profile and efficiency as a function of energy used in this work match that of the Dexela 1512 flat panel detector.[38,39] This was chosen due to the authors' familiarity with this particular detector, its success in use at commissioned LCSs,[17,40] and its use as a mammographic imaging camera,[38] however any detector may be used. For simplicity, it was assumed the detector had a constant temperature over each exposure and that the signal response was within the linear regime. The properties of the detector are summarized in Table 1. This detector was used for all imaging simulations performed within this study.

A 0.3-mm carbon anti-scatter grid based on reported energy-angle filtering simulations[41] was applied. An air gap of 1.5 cm between the phantom and detector was used for all simulations. The source to image distance for the CEM simulations was 65 cm while for the laser-Compton simulations was 25 m. The large distance from the interaction point for the LCS simulations here is necessary since the natural divergence of the beam is small on the order of 1–4 mrad. Due to the highly collimated nature of the Compton source, this could allow for placement of the detector further away from the patient, thereby reducing noise due to scattering off tissue eliminating the need for a grid filter. Since this is not common in traditional imaging, this was not applied and the same object-to-detector distance was used in all simulations for accurate and direct comparisons. The resolution of the simulations here is 200 μm × 200 μm.

TABLE 1 Properties of the Dexela 1512 detector used for the imaging simulations in this study.[38,39]

Detector property	Value
Scintillator	200 μm CsI
Dark current	6 pA/cm^2
Conversion gain	119.6 e$^-$/DN
Read noise	360 e$^-$ rms

Abbreviations: CsI, cesium iodide; DN, digital number; rms, root-mean-square.

Flat-field/flux correction was applied to each high- and low-energy exposure image. At this stage, one could consider the individual exposures of the raw images before dual-energy reconstruction. Two KES reconstruction protocols were used. The first is simple subtraction computed as

$$\mathrm{KES} = \mathrm{LE} - \mathrm{HE},$$

where LE and HE are the flat-field corrected low-energy and high-energy images, respectively. The second is the CEM standard weighted log subtraction (wKES),

$$\mathrm{wKES} = -\ln(\mathrm{HE}) + w\ln(\mathrm{LE})$$

where w is a material-dependent weighting factor that serves to shift the signal to make the signal of the surrounding tissue as minimal as possible to boost the contrast in the reconstructed wKES image.[42] While simple subtraction is done with the transmission images, wKES is a subtraction between absorption images with a scaling (weighting) factor on one of the images. For a monoenergetic energy spectrum, the weighting factor is the ratio of the mass attenuation factor, μ/ρ, due to the surrounding tissue at high and low energy, $w = (\mu/\rho)_{HE}/(\mu/\rho)_{LE}$.[42] For the polyenergetic bremsstrahlung and quasimonochromatic Compton spectra used in this study, the weighting factor was computed using the effective attenuation factor, $(\mu/\rho)^{\mathrm{eff}}$, for the high- and low-energy exposures,

TABLE 2 Properties of the four phantoms used in this study.

BI-RADS classification	Fibroglandular tissue fraction	Mean compressed thickness (cm)
Almost entirely fatty (a)	0.05	4.7
Scattered fibroglandular (b)	0.15	4.2
Heterogeneously dense (c)	0.34	4.2
Extremely dense (d)	0.60	4.2

$w = (\mu/\rho)^{\text{eff}}_{HE}/(\mu/\rho)^{\text{eff}}_{LE}$, where

$$(\mu/\rho)^{\text{eff}} = \frac{\int (\mu/\rho)(E)\,\phi(E)\,dE}{\int \phi(E)\,dE}.$$

Here, ϕ is the integrated spectrum of the x-ray source as a function of energy, E. Soft tissue was chosen as the surrounding material to simultaneously capture the fibroglandular, skin, adipose, and vascular tissues, and the corresponding attenuations were obtained from the National Institute of Standards and Technology (NIST).[43] The weighting factors for CEM, DET, and SKES were determined to be 0.2077, 0.9704, and 0.9685, respectively.

CEM typically includes additional modifications to the image in the post-processing stage to enhance the contrast of the image. Some of these operations include thresholding, segmentation, nonlinear histogram weighting/equalization, gamma adjustment, and other filters. These operations apply nonlinear transformations that are unique to each image thereby rendering any direct comparison of the contrast difference between the different x-ray sources no longer one-to-one. Therefore, any additional post-processing beyond flat-field correction, simple subtraction, or weighted log subtraction was not performed.

2.4 | Breast phantom

The VICTRE breast phantom process was used to generate the computational phantoms in this study.[44] This was chosen for its anatomical realism, randomization, inclusion of tumors, and finite element mechanical compression capabilities. Densities and elemental compositions of the materials in the phantoms were obtained from NIST and elsewhere in the literature.[43,45] Four phantoms were randomized for this study, one of each BI-RADS density classification. Table 2 summarizes the glandularity and compression thickness of each of the phantoms. All phantoms were compressed in craniocaudal (CC) view with lexan compression paddles that remained in the phantom at the x-ray propagation phase. To improve computational speed, only the portion of the phantom anterior to the pectoralis muscle was imaged. This field-of-view is characteristic of a traditional CC mammogram. Extra air space anterior to the phantoms was also not imaged to improve computation speed and memory usage.

Each phantom contained four lesions placed at randomly selected terminal duct lobular units (TDLUs). These lesions are all identical and contain iodine at concentrations of 0.1% m (1.02 mg/cc) and 0.5% m (5.1 mg/cc). The lower concentration represents a weakly enhancing tumor while the higher concentration represents a strongly enhancing one. These concentrations were determined from reported areal density of iodine contrast in various breast lesions in the literature and calculated for tumors 0.5–2 cm in size.[46]

The four randomly generated breast phantoms are presented in Figure 3 with their respective density classifications. The placement algorithm for lesion insertion of the VICTRE phantom protocol happened to favor anterior placement of tumors in these phantoms, especially for the primarily fatty phantom. This is considered acceptable for this proof-of-principle study, though in the future, placement randomization should be weighted to the lesion distribution that is observed in the population. As for general morphology, the less fibroglandular tissue present in the phantom, the larger the phantom size, resulting in variable path lengths following finite element compression (see Table 2).

2.5 | Dose determination and contrast metrics

Calculation of mean glandular dose (MGD) for each phantom/source combination was performed by means of Monte Carlo simulations using TOPAS version 3.9.[47] TOPAS is a wrapper and extender of the Monte Carlo software Geant4 which has been validated for MGD calculations and general dosimetry extensively in the literature.[48–51] The dose for both high- and low-energy exposures were simulated. Ten million photons were used in each of these simulations and the total dose per photon to the glandular tissue was scored. Each simulated exposure was repeated 10 times.

Two image quality metrics were used in this analysis. The CNR of the KES image is defined by

$$\text{CNR} = \frac{\mu_t - \mu_s}{\sqrt{\sigma_t^2 + \sigma_s^2}},$$

where μ is the mean signal and σ^2 is the variance of the signal. The subscripts t and s represent the tumor and the surrounding tissue, respectively. Here, the surrounding tissue is a circular annulus around the lesion of equal area as the lesion. The relative contrast ratio (RCR),[20] also known as the Weber contrast,[52] of the KES image

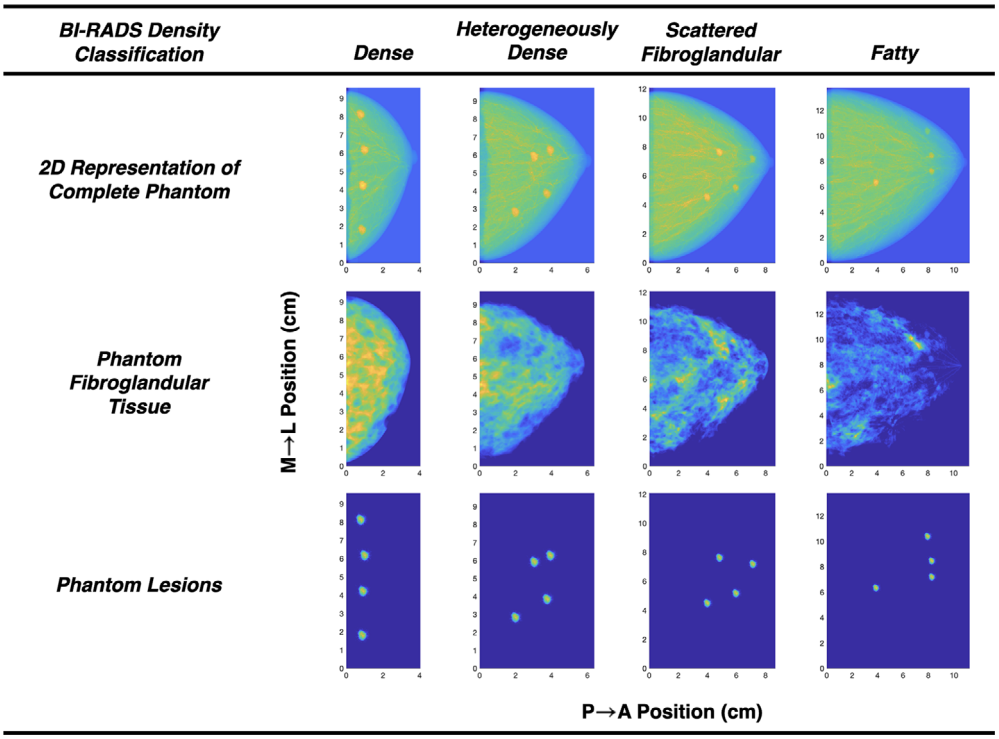

FIGURE 3 Graphical summary of breast phantoms used in this study including their morphology, distribution of fibroglandular tissue, and tumor/lesion placement.

is defined by

$$\mathrm{RCR} = \left| \frac{\mu_t - \mu_s}{\mu_s} \right|.$$

These two contrast metrics were averaged over the four lesions and reported as a single value.

Since the MGD is an important measure that contributes to both the image quality and the safety limitations of the study, both contrast metrics were normalized to the dose. Explicitly, these definitions are CNRD = CNR/MGD and RCRD = RCR/MGD. Also included in this analysis is the figure-of-merit (FOM) that has been used most often in mammographic imaging, which is the ratio of the square of the CNR to the MGD, FOM = CNR^2/MGD. The inverse metrics are also important (DCNR = MGD/CNR and DRCR = MGD/RCR), as they paint the data from the perspective of dose reduction instead of contrast enhancement. The ratio of these metrics to a clinical dual-energy image gives insight into an increase (ratio > 1) or a decrease (ratio < 1) compared to what is currently available today. These metrics are defined as,[20]

$$\mathrm{rCNRD} = \frac{\mathrm{CNRD_{LCS}}}{\mathrm{CNRD_{CEM}}}, \quad \mathrm{rRCRD} = \frac{\mathrm{RCRD_{LCS}}}{\mathrm{RCRD_{CEM}}}$$

$$\& \quad \mathrm{rFOM} = \frac{\mathrm{FOM_{LCS}}}{\mathrm{FOM_{CEM}}}$$

where the subscript LCS refers to either DET or SKES and the subscript CEM refers to the conventional dual-energy bremsstrahlung tube source. These quantities were determined for both simple subtraction and weighted log subtraction reconstruction methods.

3 | RESULTS

The integrated spectra of each of the sources are presented in Figure 4. The conventional dual-energy mammography source spectra are broad in bandwidth and have mean energies significantly far in energy from the K-edge. The flux of the high-energy spectrum is about 26% of the low-energy one. Both LCS spectra have much narrower BWs near the iodine K-edge. The FWHM BWs for both the high-energy and low-energy tunings of the DET spectra are 1.1% and each has an equal total flux. For SKES the total BW for the high-energy spectrum was 0.5% and 2.6% for the low-energy one, making an average of 1.6% BW across the two. The low-energy spectrum for SKES had an effective flux that is 80% of the high-energy spectrum.

For SKES, the scanning exposure protocol leads to variation in flux and effective spectra that the phantom is exposed to in the dimension orthogonal to and in the plane of the scanning dimension. To see this, Figure 5 plots spectra at constant θ_y. There is little variation in the BW for both high- and low-energy spectra across

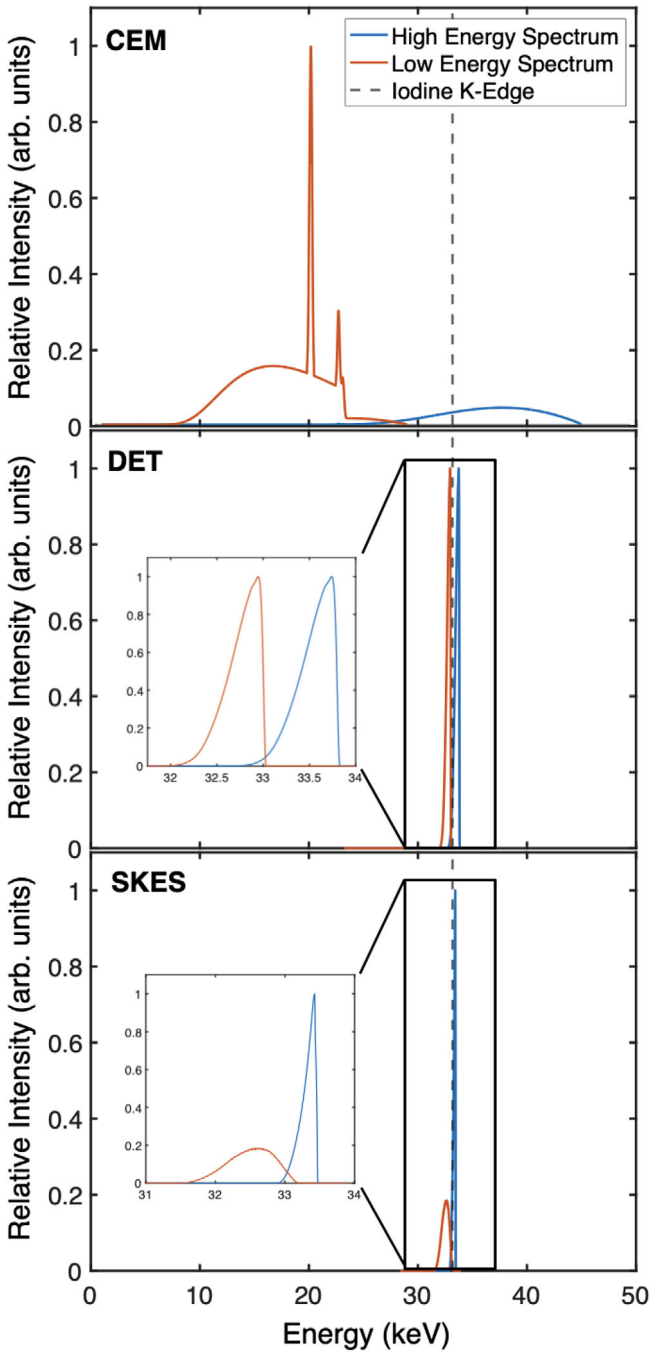

FIGURE 4 Comparison of spectra between the three methods investigated in this study and their proximity to the iodine K-edge. The spectra are normalized to peak intensity for each respective x-ray source.

varying θ_y. The flux of the high-energy spectrum varies the most normal to the scanning dimension, having the highest flux directly on-axis and decreasing flux moving away from the center.

A comparison of the MGD between each phantom and spectra/imaging methods is summarized in Table 3. The MGD using a CEM spectrum is within the range reported experimentally in the clinical literature.[37] In general, the denser phantoms had a higher MGD than the less dense ones. This trend is broken in the fatty phantom that had a higher dose than the heterogeneously dense and scattered fibroglandular phantoms. The dense phantom had the highest dose overall for every imaging method investigated here. The dose between the direct energy tuning and SKES methods is approximately the same. There is a very minor (<0.5%) increase in dose from SKES compared to DET. The LCS spectra provide around a 20% dose decrease compared to the current clinically implemented modality across the board.

A demonstration of the KES reconstruction from high-energy and low-energy exposures is shown for the case with low-enhancing tumors in the dense phantom is shown in Figure 6. Figure 7 shows a graphical summary of the simulation results with the reconstructed

TABLE 3 Mean glandular dose for different spectrum/phantom combinations.

Spectrum	Phantom	Energy	MGD (mGy)	Combined MGD (mGy)
CEM	D	HE	0.9509 ± 0.0010	2.6826
		LE	1.7317 ± 0.0009	
	HD	HE	0.8812 ± 0.0010	2.3098
		LE	1.4286 ± 0.0010	
	SF	HE	0.8893 ± 0.0014	2.1794
		LE	1.2901 ± 0.0016	
	F	HE	0.9340 ± 0.0026	2.2086
		LE	1.2746 ± 0.0023	
DET	D	HE	1.0320 ± 0.0007	2.0989
		LE	1.0669 ± 0.0015	
	HD	HE	0.9514 ± 0.0013	1.9307
		LE	0.9793 ± 0.0013	
	SF	HE	0.9547 ± 0.0015	1.9340
		LE	0.9793 ± 0.0020	
	F	HE	0.9965 ± 0.0024	2.0171
		LE	1.0206 ± 0.0025	
SKES	D	HE	1.0430 ± 0.0018	2.1207
		LE	1.0777 ± 0.0007	
	HD	HE	0.9605 ± 0.0019	1.9462
		LE	0.9857 ± 0.0014	
	SF	HE	0.9597 ± 0.0011	1.9473
		LE	0.9876 ± 0.0015	
	F	HE	1.0050 ± 0.0014	2.0335
		LE	1.0285 ± 0.0022	

Note: A photon fluence of 4.18×10^9 ph cm^{-2} was used for all studies. A total of 10 simulations were performed for each dose determination with the mean MGD ± the standard deviation given.

Abbreviations: CEM, contrast-enhanced mammography; D, dense; DET, direct energy tuning method; F, fatty; HE, high energy; HD, heterogeneously dense; LE, low energy; MGD, mean glandular dose; SF, scattered fibroglandular; SKES, scanning K-edge subtraction.

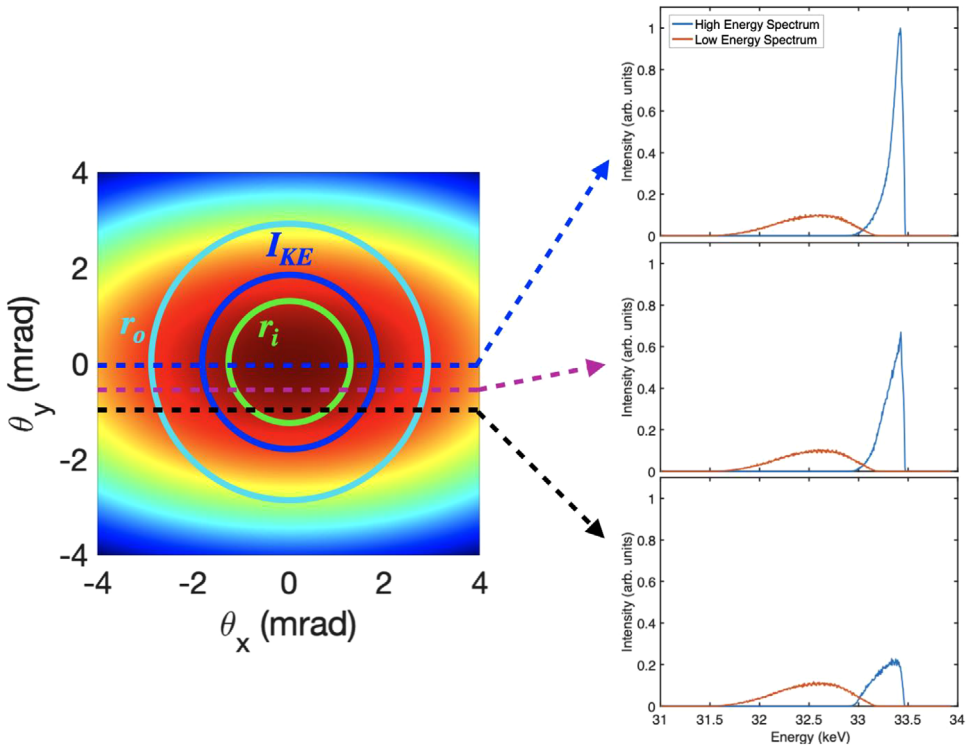

FIGURE 5 Illustration of spectral variation in the dimension normal to the scanning dimension. The low-energy spectrum has little variation while the high-energy spectrum changes more in flux than it does in bandwidth.

dual-energy images using simple subtraction for the three different modalities investigated in this study. Low-enhancing tumors are not easily seen using CEM sources, but they are easily identifiable using an LCS in both direct energy tuning and scanning modes. The tumors are identifiable in every source type if they are strongly enhancing ([I] = 5.1 mg/cc), highlighting the usefulness of clinical contrast-enhanced mammography. In this strongly enhancing case, both LCS modalities have a much larger contrast compared to the conventional dual-energy source making the tumors much more identifiable. In both concentrations of iodine shown in the figure, the two LCS modalities have comparable enhancement. The scanning configuration resulted in vertical artifacts in the scanning dimension with increasing noise moving posteriorly or anteriorly from the centroid of the phantom.

Two contrast metrics were used to analyze image quality and detectability of tumors between the three modalities investigated and are defined above. The average RCR, CNR, and FOM of the four tumors in each scenario using simple subtraction reconstruction are presented in Table 4. In CEM, the dense phantom had the worst relative contrast. Comparing the two LCS methods, DET had higher RCR but lower CNR than SKES for every phantom. Both LCS methods had markedly larger RCR (25×–32×), larger CNR (2×–3×), and larger FOM (6×–16×) compared to CEM. Between the two concentrations of iodine contrast, there is an observed ∼5× increase in RCR for both LCS methods and <5× for CEM. For CNR, there is a 2–3 times increase for every modality increasing the iodine concentration from 1.02 mg/cc to 5.1 mg/cc. Similarly, all three imaging modalities had an approximate 6–7× increase in FOM when increasing the iodine concentration from low to high.

The data presented in Table 5 shows the comparison of the dose-normalized metrics between DET/SKES and CEM by taking their ratios. When accounting for both the contrast increase and dose decrease provided by the two LCS methods simultaneously, LCS can provide a >60x improvement compared to CEM. The RCRD improvement for both LCS methods is greater for more dense phantoms compared to less dense ones. RCRD saw a greater increase for DET, while CNRD had a 10%–30 % greater increase in the scanning configuration when comparing dense to fatty phantoms. A greater concentration of iodine contrast, in general, resulted in larger rRCRD, rCNRD, and rFOM.

A comparative analysis using the weighted log subtraction for KES reconstruction was also performed. Figure 8 shows the graphical summary using this reconstruction method, and the corresponding image quality and dose metrics are shown in Tables 6 and 7. The trends in RCR and CNR were relatively the same for the weighted reconstruction as compared to the

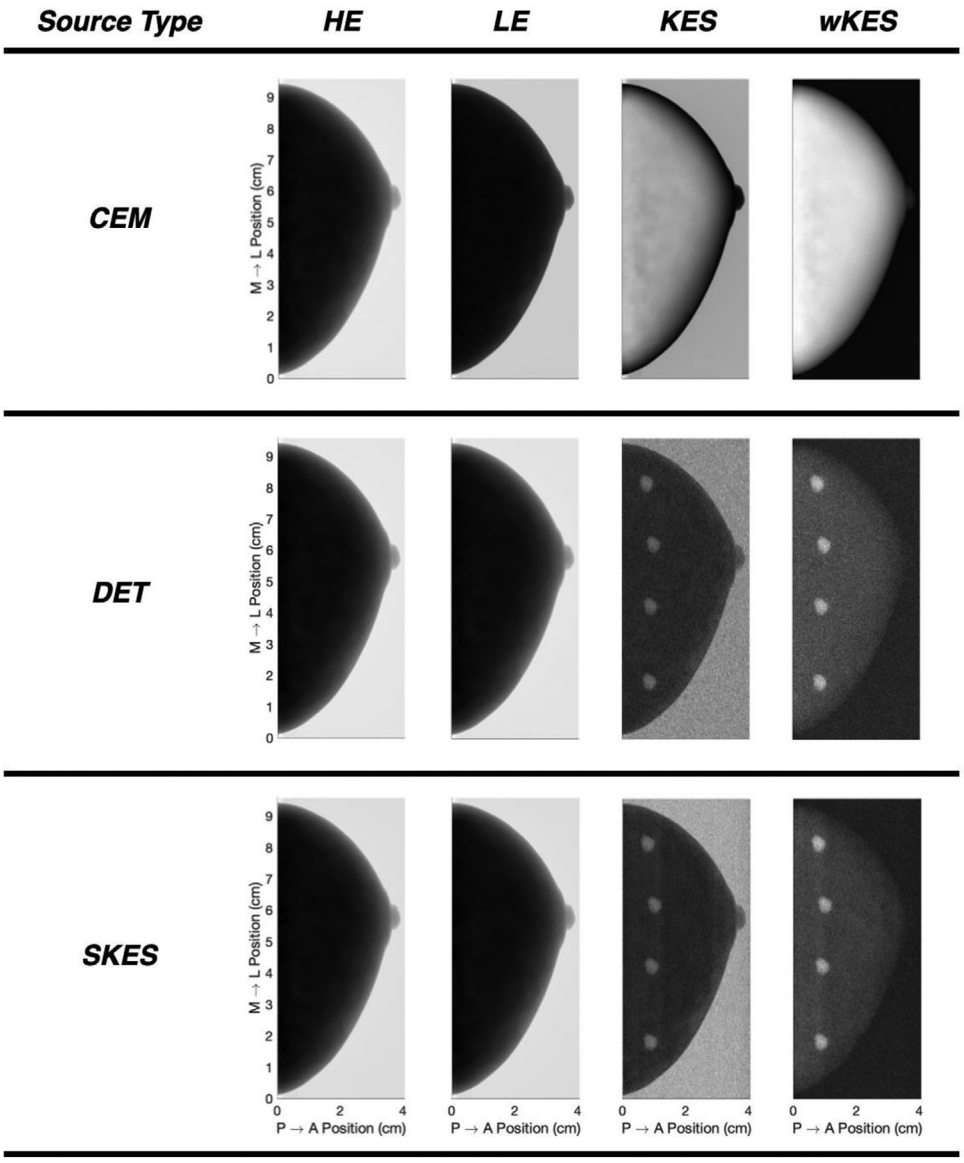

FIGURE 6 Single energy images (HE/LE) along with combined KES images for the dense phantom simulations with 1.02 mg/cc iodine tumors under simple subtraction reconstruction (KES) and weighted log subtraction reconstruction (wKES). The only post-processing applied to the single exposure HE/LE images was flat-field correction. HE, high energy; KES, K-edge subtraction; LE, low energy.

simple subtraction reconstruction. CNRs were mostly unchanged when using weighted log subtraction compared to simple subtraction, with a variation between 1% and 10% observed. Similarly, the FOMs saw small variations compared to simple subtraction. When using weighted log subtraction, RCRs for CEM decreased by 15× when compared to simple subtraction. The RCRs for DET and SKES also decreased but by larger amounts, approximately 30× for DET and 20× for SKES.

The use of weighted subtraction had concomitant changes in the dose-normalized contrast metrics as seen in Table 7 when compared to Table 5. rCNRD saw only a slight decrease in the weighted log subtraction reconstruction vs the simple subtraction reconstruction, as expected with the only minor changes in CNR. rRCRD had the largest changes with DET losing about half of the improvement over CEM, but remains up to 28× improvement in dose-normalized contrast compared to CEM. Similarly, SKES lost between 25% and 35% rRCRD when using weighted log subtraction as opposed to simple subtraction, though it remains up to 30× better than CEM. The FOM for SKES was on the order of 10x larger than CEM, while DET had a 7–9× increase over CEM.

Looking at Figure 8, there are noticeable differences and similarities when comparing to the simple subtraction images in Figure 7. The detectability of the lesions was not changed when using weighted log

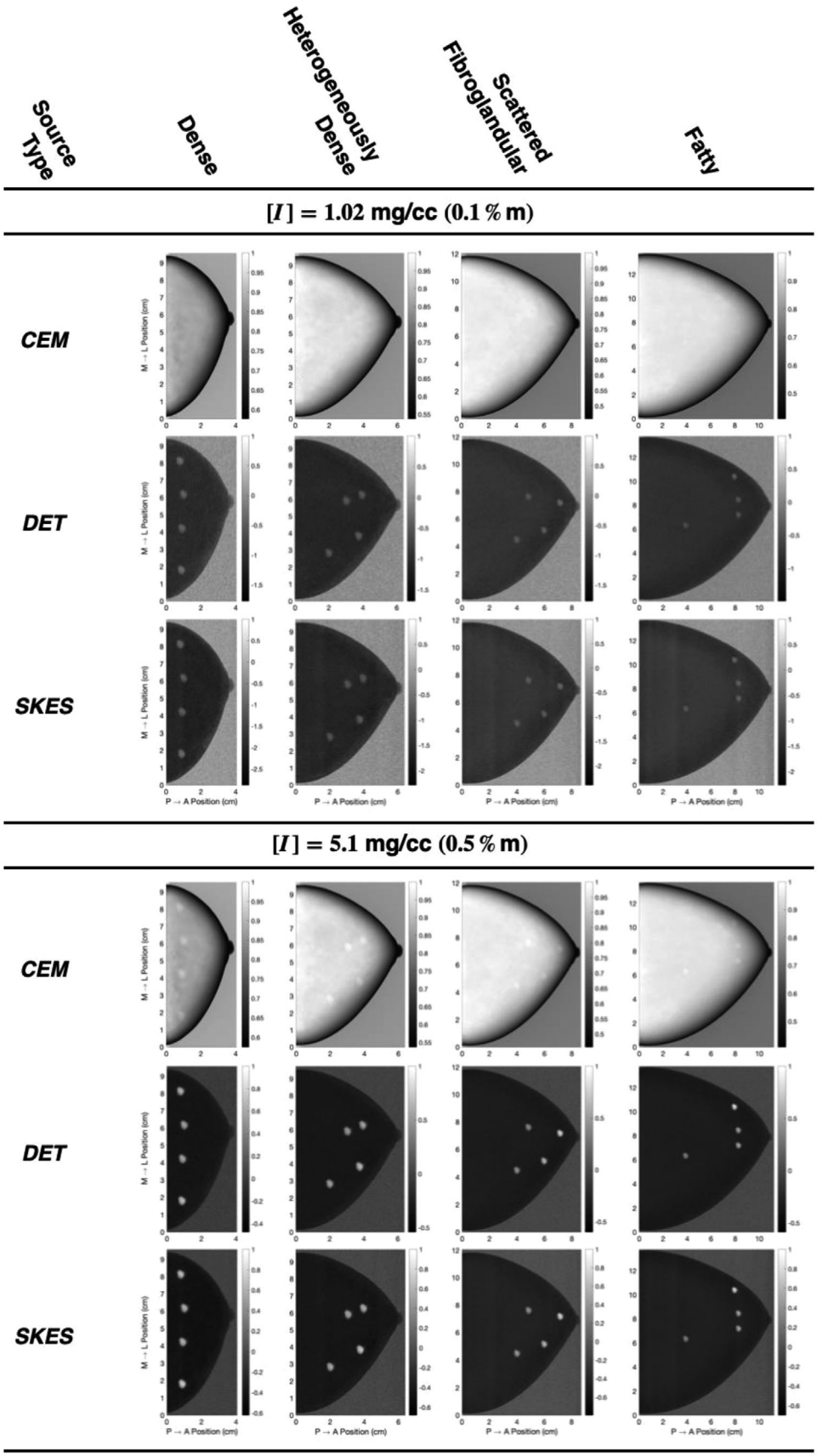

FIGURE 7 Summary of KES images for each phantom and x-ray source investigated for two different lesion concentrations of iodine contrast using simple subtraction reconstruction. Each image has been normalized to have unity peak value. KES, K-edge subtraction.

TABLE 4 Relative contrast ratios, contrast-to-noise ratios, and figures-of-merit of each spectrum/phantom combination for the simple subtraction reconstruction method.

	CEM			DET			SKES		
Phantom	**RCR**	**CNR**	**FOM**	**RCR**	**CNR**	**FOM**	**RCR**	**CNR**	**FOM**
[I] = 1.02 mg/cc (0.1%m)									
D	0.018	1.255	0.587	0.584	2.871	3.926	0.455	3.743	6.612
HD	0.021	0.860	0.320	0.502	2.649	3.637	0.416	3.149	5.101
SF	0.024	0.834	0.319	0.477	2.478	3.185	0.392	2.757	3.907
F	0.027	1.066	0.514	0.483	2.400	2.859	0.416	2.534	3.163
[I] = 5.1 mg/cc (0.5%m)									
D	0.058	3.402	4.314	2.870	7.203	24.72	2.221	8.093	30.91
HD	0.059	2.218	2.129	2.452	7.261	27.32	2.015	8.116	33.88
SF	0.062	2.005	1.841	2.338	7.171	26.66	1.930	7.647	30.05
F	0.064	2.242	2.273	2.406	7.087	24.93	2.061	7.303	26.26

Note: Values are averaged across all 4 lesions within each phantom.
Abbreviations: CEM, contrast-enhanced mammography; CNR, contrast-to-noise ratio; D, dense; DET, direct energy tuning method; F, fatty; FOM, figure-of-merit; HD, heterogeneously dense; MGD, mean glandular dose; RCR, relative contrast ratio; SF, scattered fibroglandular; SKES, scanning K-edge subtraction.

TABLE 5 Summary of dose-normalized contrast metrics relative to the CEM spectrum for the simple subtraction reconstruction method.

	DET			SKES		
Phantom	**rRCRD**	**rCNRD**	**rFOM**	**rRCRD**	**rCNRD**	**rFOM**
[I] = 1.02 mg/cc (0.1%m)						
D	40.4	2.92	6.69	31.2	3.78	11.3
HD	28.7	3.69	11.4	23.7	4.35	15.9
SF	22.4	3.36	9.99	18.2	3.71	12.3
F	19.9	2.47	5.56	17.0	2.59	6.15
[I] = 5.1 mg/cc (0.5%m)						
D	63.4	2.71	5.73	48.6	3.01	7.17
HD	49.4	3.92	12.8	40.3	4.35	15.9
SF	42.8	4.05	14.5	35.0	4.28	16.3
F	41.2	3.47	11.0	35.0	3.55	11.6

Abbreviations: CEM, contrast-enhanced mammography; CNR, contrast-to-noise ratio; D, dense; DET, direct energy tuning method; F, fatty; FOM, figure-of-merit; HE, high energy; HD, heterogeneously dense; RCR, relative contrast ratio; SF, scattered fibroglandular; SKES, scanning K-edge subtraction.

subtraction as the 1.02 mg/cc iodine lesions are still not as detectable in CEM as they are in DET and SKES. Because these images are now log-transformed, the background air around the phantom no longer has a value near zero for both the LCS methods. However, the signal difference between the background tissue and background air has decreased for weighted log subtraction, providing an image that is perceptively high in contrast to the human observer, especially for the high iodine concentration simulations.

4 | DISCUSSION

CEM was not able to reliably identify low-enhancing tumors ([I] = 1.02 mg/cc). Moreover, CEM had worse contrast in more dense phantoms compared to the less dense ones. This paints the clinical reality where mammograms of patients with dense breasts have lower diagnostic power. Laser-Compton scattering, on the other hand, in both DET and scanning configurations, is easily able to detect both low-enhancing lesions and lesions within dense phantoms all while depositing less glandular dose. In fact, in the phantoms simulated in this study, both LCS configurations had generally higher RCR, CNR, and FOM for denser phantoms than less dense ones. These results further indicate that LCSs can be a solution to improve mammography in the at-risk population.

The broad bandwidths of the CEM spectra limit the concentration of iodine that is visible upon KES. Ideally, to obtain the most contrast, two monoenergetic spectra with one just above and another just below the K-edge of the contrast element would be used. Such an ideal scenario is currently not possible using traditional x-ray tubes. LCSs provide the tunability and narrow bandwidths to enhance this contrast allowing for much smaller concentrations of iodine, and therefore weakly enhancing tumors, to be more easily identified.

A concomitant feature of having narrow bandwidths close in energy is the improvement in background subtraction. This is because the linear attenuation of material becomes closer to constant as the effective energy of spectra gets closer together. Combined with an increasing ratio of attenuation due to the contrast agent's K-edge gives a stronger contrast. However, complete removal of the background, as is observed in DET and SKES in Figures 6 and 7, may not be clinically desirable since anatomical insight from surrounding structures could provide useful information to the clinician. It is conceivable, that in a DET configuration, one could obtain a third image that has x-ray energy tuned to the characteristic Kα energy of rhodium or

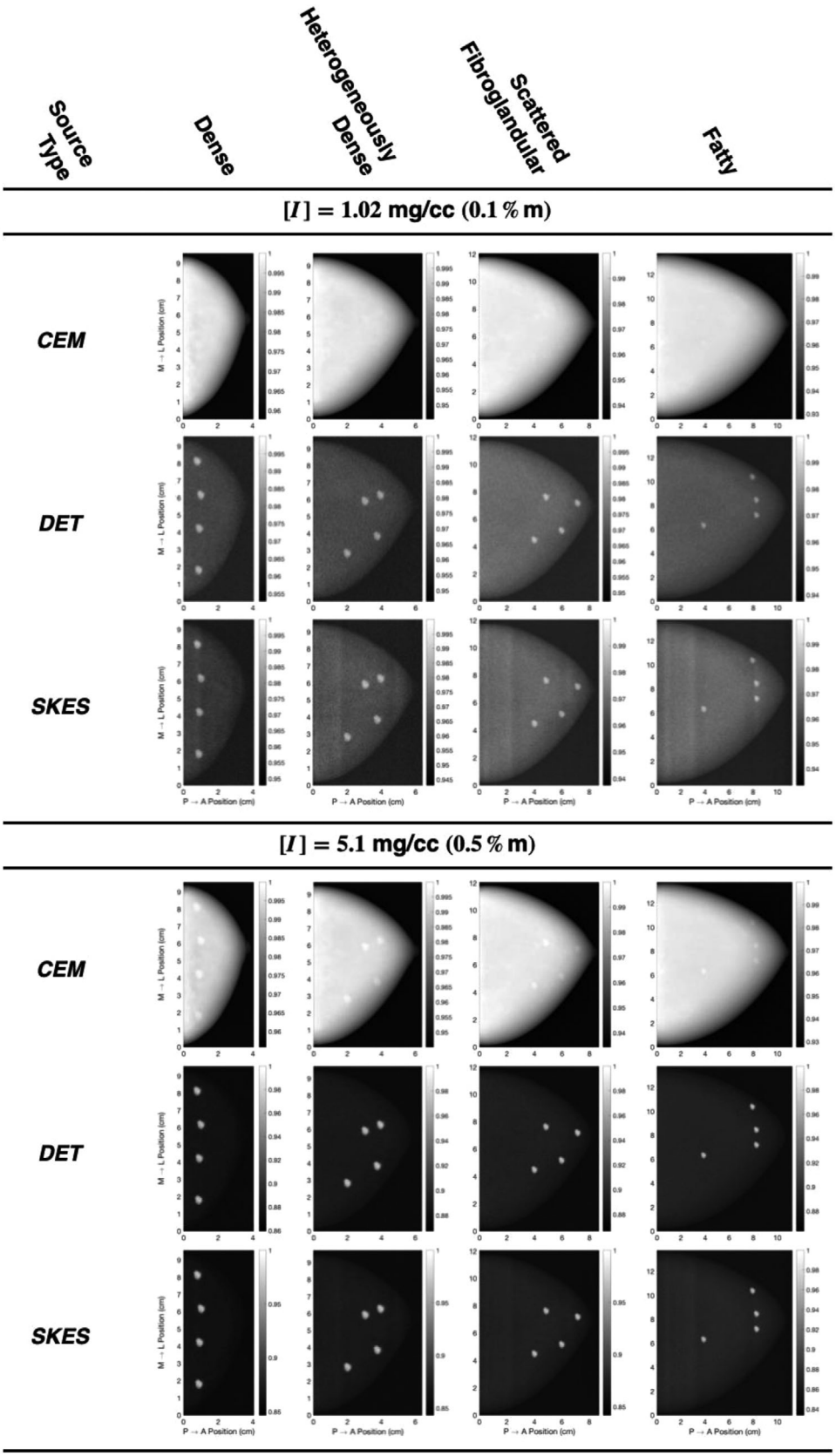

FIGURE 8 Summary of wKES images for each phantom and x-ray source investigated for two different lesion concentrations of iodine contrast using weighted log subtraction reconstruction. Each image has been normalized to have unity peak value. KES, K-edge subtraction.

TABLE 6 Relative contrast ratios, contrast-to-noise ratios, and figures-of-merit of each spectrum/phantom combination for the weighted log subtraction reconstruction method.

	CEM			DET			SKES		
Phantom	**RCR**	**CNR**	**FOM**	**RCR**	**CNR**	**FOM**	**RCR**	**CNR**	**FOM**
[I] = 1.02 mg/cc (0.1%m)									
D	0.00120	1.219	0.554	0.0170	2.915	4.049	0.0193	3.340	5.266
HD	0.00138	1.008	0.440	0.0165	2.718	3.829	0.0192	2.881	4.268
SF	0.00150	0.993	0.373	0.0149	2.372	2.918	0.0176	2.602	3.478
F	0.00155	0.992	0.445	0.0150	2.534	3.186	0.0177	2.388	2.809
[I] = 5.1 mg/cc (0.5%m)									
D	0.00423	3.606	4.848	0.0930	6.894	22.64	0.1065	7.630	27.48
HD	0.00440	2.690	3.131	0.0880	7.135	26.38	0.1045	7.612	29.81
SF	0.00455	2.419	2.682	0.0845	7.002	25.42	0.1005	7.467	28.64
F	0.00454	2.443	2.699	0.0827	6.914	23.72	0.0992	7.381	26.83

Note: Values are averaged across all 4 lesions within each phantom.
Abbreviations: CEM, contrast-enhanced mammography; CNR, contrast-to-noise ratio; D, dense; DET, direct energy tuning method; F, fatty; FOM, figure-of-merit; HE, high energy; HD, heterogeneously dense; RCR, relative contrast ratio; SF, scattered fibroglandular; SKES, scanning K-edge subtraction.

TABLE 7 Summary of dose-normalized contrast metrics relative to the CEM spectrum for the weighted log subtraction reconstruction method.

	DET			SKES		
Phantom	**rRCRD**	**rCNRD**	**rFOM**	**rRCRD**	**rCNRD**	**rFOM**
[I] = 1.02 mg/cc (0.1%m)						
D	18.0	3.06	7.31	20.3	3.47	9.51
HD	14.3	3.23	8.70	16.5	3.40	9.70
SF	11.3	2.97	7.82	13.2	3.23	9.32
F	10.6	2.80	7.15	12.5	2.62	6.31
[I] = 5.1 mg/cc (0.5%m)						
D	28.1	2.44	4.67	31.8	2.68	5.67
HD	24.0	3.18	8.42	28.2	3.36	9.52
SF	21.5	3.28	9.48	25.3	3.46	10.7
F	20.0	3.11	8.79	23.8	3.29	9.94

Abbreviations: CEM, contrast-enhanced mammography; CNR, contrast-to-noise ratio; D, dense; DET, direct energy tuning method; F, fatty; FOM, figure-of-merit; HE, high energy; HD, heterogeneously dense; RCR, relative contrast ratio; SF, scattered fibroglandular; SKES, scanning K-edge subtraction.

molybdenum to obtain a traditional mammographic image. Since this source will contain only that energy and no other lower energies typically generated from the bremsstrahlung process, such a mammographic image will be lower in dose, higher in resolution, and better in contrast than one from a traditional x-ray tube. In a scanning configuration, the traditional mammographic image may be obtained by using a larger viewing angle of the x-rays and selecting a third region with lower energy x-rays to generate the mammographic image. A KES image can then be superimposed on top of the traditional mammographic image all with less dose than a traditional single view mammogram.

The variability in flux in the direction normal to scanning leads to noise variation observed in the SKES images. At these energies of Compton scattering (~30 keV), the flux variation can be up to 25% (see Figure 1c). A horizontal polarization mode was used for this study to reduce this variation to < 8%, yet this difference in flux still results in a noticeable increase in noise on the edges of the image. Furthermore, in the SKES images, this flux variation resulted in linear artifacts in the medial-to-lateral scanning dimension that remained even after flat-field correction. These artifacts can be mitigated through other post-processing techniques, similar to ring artifacts in computed tomography. Despite these potential drawbacks, the image quality of SKES was superior to that of CEM.

The narrow-bandwidth LCS has an observed decrease in dose compared to the broad-bandwidth conventional source. The decrease is primarily due to elimination of low-energy photons that are present in the low-energy rhodium-filtered spectrum in the CEM source. These low-energy photons, especially those 10 keV and below, rarely penetrate the phantom and induce scintillation in the detector after passing through material. These photons act to only increase dose as they rarely contribute to the statistics of the image. The minute increase in dose (<0.5%) from SKES compared to DET is due to its broader bandwidth effective low-energy spectrum introducing lower energies that tend to deposit more dose. Regardless of this minute increase, the doses between DET and SKES for all phantoms are approximately the same since the mean energies and energy bandwidths of the spectra are very similar. As a general trend across all phantoms, the high-energy exposure deposits less dose than the low-energy exposure. This is attributable to the known decrease in dose with increasing x-ray energy within the energy range of this study. The difference in dose between high and low energies is more prominent for CEM than the two LCS modalities, explained by the difference in mean energy. For CEM, the mean energies of high- and low-energy

exposures are 36.5 and 17.7 keV, respectively, making a difference of 18.8 keV. For DET, the mean energy for high- and low-energy exposures respectively are 33.5 and 32.8 keV, and for SKES the values respectively are 33.3 and 32.5 keV. For the LCS modalities, this makes a difference in energy of only 0.7 keV for DET and 0.8 keV for SKES, thereby explaining the similarity in dose between these two methods.

In general, for biological material, the dose per transmitted photon decreases until a minimum around of 60–70 keV until it starts increasing again.[20] For this reason, KES using LCSs, in either direct energy tuning or scanning modes, would improve if contrast agents with K-edge energies within range of this minimum were used. Currently, only iodine and gadolinium have been considered since both of those contrast agents are used clinically. Iodine has the advantage of greater tumor uptake of the contrast, however, gadolinium has significantly lower rates of adverse effects and a lower risk of severe reactions.[53,54] Gadolinium also has a K-edge that is closer to the dose minimum (50.2 keV) making it more dose-favorable for KES. If tunable and narrow-bandwidth sources like LCSs become a standard in clinical radiography, it may be useful to design contrast agents that take advantage of the dose minimization and contrast enhancement properties enabled by them. Additionally, if higher energy contrast agents are used, this could enable the implementation of KES mammography without compression due to lower tissue attenuation of x-rays at higher energies. In fact, it was shown previously in a computational study that KES performs better in thicker phantoms.[55]

Both DET and SKES are able to detect lesion contrast uptake that was not detectable using a CEM source. Tumors that CEM can detect have higher contrast using LCS methods. The improvement is quantifiably drastic in both relative contrast and metrics that include the noise, like contrast-to-noise.

When comparing contrast metrics under simple subtraction reconstruction, it is observed that SKES has a larger CNR yet lower RCR compared to DET. This can be explained by the effective spectra between the two configurations. The DET spectra are less varying, meaning they have similar profiles and the same fluxes but different energies. The capability to tune the source to the desired energies allows for better background subtraction and contrast enhancement leading to a larger RCR, and since the background subtraction is closer to zero, the noise tends to be more variable due to this signal floor. The variability in the SKES spectrum results in slightly less relative contrast. Concomitantly, the background subtraction is not as close to zero in this case leading to a smaller variance in signal (i.e. noise) and thus having better CNR compared to DET. It is possible to have an alternative objective for Bayesian optimization, one that maintains equal bandwidth for the high-energy and low-energy effective spectra as opposed to one that maintains total bandwidth to within some tolerance to close this gap in contrast and noise to make the two methods even more equivalent. Ultimately, in the configuration studied here, the two methods are indeed comparable to one another.

It is observed that rRCRD had the most improvement for denser phantoms compared to ones with a high fraction of adipose tissue. This is likely due to the fact that CEM has a difficult time detecting tumors which notoriously hide within dense fibroglandular regions of the breast tissue. As such, there is a larger improvement when moving to a LCS. For these dense phantoms, the improvement can be greater than 60× in the DET mode or nearly 50× in SKES. This means that laser-Compton scattering KES can produce an image with the same contrast as a CEM image with only 1.7% of the dose in DET mode, or 2% of the dose in scanning mode under the approximation of linearity upon inversion of the metric. As such, this has the potential to extend the clinical benefit to the entire population, including imaging of other organs, not just in mammography.

When performing KES imaging the subtraction operation is detrimental for two reasons: (1) it lowers the effective signal, and (2) the statistical noise is still additive. Thus, to get KES imaging to work, one needs to maximize the relative difference in signal within the zone of contrast uptake so that sufficient signal remains following the subtraction operation. In terms of x-ray sources, this naturally leads to a tunable and narrow bandwidth solution that LCS offers.

The industry standard weighted log subtraction reconstruction was also employed in this study. The weighting factors for the two LCS methods, DET ($w = 0.9704$) and SKES ($w = 0.9685$) are similar in value since their respective high- and low-energy x-ray spectra are close in mean energy and energy bandwidth. Moreover, their weighting factors are close to unity since the difference in mean energy is small between the high- and low-energy exposures within each modality. A weighting factor equal to 1 would mean the two tunings have the same energy and the background tissue will be perfectly subtracted. Comparing the intensity of the backgrounds between CEM and the two LCS methods in Figure 8, it is observed DET and SKES have significantly better background subtraction than CEM even with the use of the weighting factor.

When analyzing the relative contrast ratio metrics using weighted log subtraction, the best improvement seen for strong enhancing tumors in DET decreases from over 60× to under 30×, and from almost 50× in SKES to just over 30×. This change is attributable to the weighted subtraction operation. The numerical effect of the weighting factor is to proportionally shift the baseline to an alternative value with the goal of making the surrounding tissue subtract closer to zero. Since the signal is shifted, the RCR metric is affected as it is a ratio of

signals. CNR, on the other hand, only has a difference of signal, so this quantity is less affected as is observed in Table 6. The net result is rCNRD also does not change substantially. Although rCNRD changed minimally, rFOM did have somewhat of a decrease using weighted log subtraction compared to simple subtraction due to the compounding effect squaring the CNR has within the definition of the FOM. Regardless, when using weighted subtraction, the contrast boost remains high, and one could obtain an image in SKES or DET at about 3% of the dose of CEM at the same relative contrast as CEM.

DET can require large distances to get full-field exposure. For example, using the 4-mrad half-angle in this study, to get a 20-cm field coverage, a source-to-object distance of 25 m would be required. In a scanning configuration, on the other hand, one could use a larger half-angle beam and place blocks at the appropriate regions to obtain the effective dual monochromatic energies. This allows for a larger field of view and permitting patient placement closer to the source. An alternative way to overcome the distance limitation is to implement a 2D pencil beam scanning procedure. The authors investigated this, and the image quality of a KES image is again comparable to the DET and 1D scanning modalities. The trade-off of a 2D scanning approach is additional movements can lead to more blurring artifacts in the image.

5 | CONCLUSION

This study looked at the feasibility of a scanning orientation in LCS, contrast-based, dual-energy imaging, and compared it to direct energy tuning of LCS and a current clinically used source. The detectability of tumors in scanning KES with an LCS is significantly improved compared to CEM sources and is comparable to DET. Quantifiably, this improvement is up to 31.8 times in the dose-normalized contrast metric, rRCRD, when using the standard weighted log subtraction reconstruction. Inverting this metric under the assumption of linearity shows that a scanning KES image with equal contrast to a CEM image can be obtained with only 3% of the dose. Moreover, the capability to identify tumors even in patients with dense breast tissue can help satisfy the need to improve mammography for this patient demographic. Since a similar image can be obtained in a scanning configuration as in a direct energy tuning one, a LCS would only need to run at a single energy tuning instead of making time-consuming alterations to the electron beam parameters between exposures. A scanning configuration would thus make clinical translation of LCSs for K-edge subtraction imaging more viable.

ACKNOWLEDGMENTS

The authors would like to thank Dr. Agnese Lagzda, Dr. Yoonwoo Hwang, Dr. Fred Hartemann, and Dr. Ferenc Raksi for providing the resources and details regarding the Compton source necessary to perform this study, Joy Yang for her illustration of the patient, and Dr. Ronald Shnier, Mauricio Quiñonez and Michael Walter Louis Seggebruch for their useful feedback on the manuscript. T. Reutershan and H.H. Effarah received partial training funding supported by the National Institutes of Health training grant number T32GM008620.

CONFLICT OF INTEREST STATEMENT

CPJB is co-founder and CTO of Lumitron Technologies, Inc. All other authors have no relevant conflicts of interest to disclose.

REFERENCES

1. Barty CPJ. Methods for 2-color radiography with laser-compton X-ray sources. US Patent 10508998, 2019.
2. Jochelson MS, Lobbes MBI. Contrast-enhanced mammography: state of the art. *Radiology*. 2021;299:36-48.
3. Sung H, Ferlay J, Siegel RL, et al. Global cancer statistics 2020: GLOBOCAN estimates of incidence and mortality worldwide for 36 cancers in 185 countries. *CA Cancer J Clin*. 2021;71:209-249.
4. Caswell-Jin JL, Sun LP, Munoz D, et al. Analysis of breast cancer mortality in the US–1975 to 2019. *JAMA*. 2024;331:233-241.
5. Wanders JOP, Holland K, Veldhuis WB, et al. Volumetric breast density affects performance of digital screening mammography. *Breast Cancer Res Treat*. 2017;162:95-103.
6. Mandelson MT, Oestreicher N, Porter PL, et al. Breast density as a predictor of mammographic detection: comparison of interval- and screen-detected cancers. *JNCI J Natl Cancer Inst*. 2000;92:1081-1087.
7. Kerlikowske K, Grady D, Barclay J, Sickles EA, Eaton A, Ernster V. Positive predictive value of screening mammography by age and family history of breast cancer. *JAMA*. 1993;270:2444-2450.
8. Mammography Quality Standards Act. Food and Drug Administration. 88 FR 15126. 2023.
9. Coffey K, Jochelson MS. Contrast-enhanced mammography in breast cancer screening. *Eur J Radiol*. 2022;156:110513.
10. Jochelson MS, Dershaw DD, Sung JS, et al. Bilateral contrast-enhanced dual-energy digital mammography: feasibility and comparison with conventional digital mammography and mr imaging in women with known breast carcinoma. *Radiology*. 2013;266:743-751.
11. Dromain C, Thibault F, Muller S, et al. Dual-energy contrast-enhanced digital mammography: initial clinical results. *Eur Radiol*. 2011;21:565-574.
12. Thomlinson W, Elleaume H, Porra L, Suortti P. K-edge subtraction synchrotron X-ray imaging in bio-medical research. *Physica Med*. 2018;49:58-76.
13. Albert F, Anderson SG, Gibson DJ, et al. Characterization and applications of a tunable, laser-based, MeV-class Compton-scattering gamma-ray source. *Phys Rev ST Accel Beams*. 2010;13:070704.
14. Günther BS. Overview on inverse Compton X-ray sources. In: Günther BS, ed. *Storage Ring-Based Inverse Compton X-ray Sources: Cavity Design, Beamline Development and X-ray Applications*. Springer Theses. Springer International Publishing; 2023:117-147.
15. Hwang Y. *Characterization and Applications of Laser-Compton X-ray Source*. PhD thesis. UC Irvine; 2018.
16. Hartemann FV, Brown WJ, Gibson DJ, et al. High-energy scaling of Compton scattering light sources. *Phys Rev ST Accel Beams*. 2005;8:100702.

17. Barty CPJ, Algots JM, Amador AJ, et al. Design, construction, and test of compact, distributed-charge, X-band accelerator systems that enable image-guided. *Front Phys*. 2024;12:1472759.
18. Kulpe S, Dierolf M, Braig E, et al. K-edge subtraction imaging for coronary angiography with a compact synchrotron X-ray source. *PLOS ONE*. 2018;13:e0208446.
19. Paternò G, Cardarelli P, Gambaccini M, Taibi A. Dual-energy X-ray medical imaging with inverse Compton sources: a simulation study. *Crystals*. 2020;10:834.
20. Reutershan T, Effarah HH, Lagzda A, Barty CPJ. Numerical evaluation of high-energy, laser-Compton x-ray sources for contrast enhancement and dose reduction in clinical imaging via gadolinium-based K-edge subtraction. *Appl Opt AO*. 2022;61:C162-C178.
21. Sun C, Wu YK. Theoretical and simulation studies of characteristics of a Compton light source. *Phys Rev ST Accel Beams*. 2011;14:044701.
22. Paternò G, Cardarelli P, Fantoni S, et al. Effect of the local energy distribution of x-ray beams generated through inverse Compton scattering in dual-energy imaging applications. *Appl Opt AO*. 2023;62:4399-4408.
23. Lindfors KK, Boone JM, Nelson TR, Yang K, Kwan ALC, Miller DF. Dedicated breast CT: Initial clinical experience. *Radiology*. 2008;246:725-733.
24. Sarno A, Mettivier G, Russo P. Dedicated breast computed tomography: basic aspects. *Med Phys*. 2015;42:2786-2804.
25. Mann RM, Cho N, Moy L. Breast MRI: state of the art. *Radiology*. 2019;292:520-536.
26. Quai E, Longo R, Zanconati F, et al. First application of computed radiology to mammography with synchrotron radiation. *Radiol Med*. 2013;118:89-100.
27. Effarah HH, Reutershan T, Lagzda A, Hwang Y, Hartemann FV, Barty CPJ. Computational method for the optimization of quasimonoenergetic laser Compton x-ray sources for imaging applications. *Appl Opt AO*. 2022;61:C143-C153.
28. Elliott RL, Baucom CC, Elliott MC, Millet EH, Jiang X. Initial experience with contrast enhanced digital mammography (SenoBright)— in a comprehensive clinical breast center. *J Cancer Ther*. 2017;8:146-154.
29. Poludniowski G, Omar A, Bujila R, Andreo P. Technical Note: SpekPy v2.0—a software toolkit for modeling x-ray tube spectra. *Med Phys*. 2021;48:3630-3637.
30. van der Geer B, De Loos M. The general particle tracer code: design, implementation and application. 2001.
31. Barty CPJ. Modulated method for efficient, narrow-bandwidth, laser Compton X-ray and gamma-ray sources. US Patent 9706631. 2017.
32. Messerly MJ, Dawson JW, Barty CPJ, Gibson DJ, Prantil MA, Cormier E. Directly driven source of multi-gigahertz, sub-picosecond optical pulses. US Patent 9166355. 2015.
33. Hartemann FV, Kerman AK. Classical theory of nonlinear Compton scattering. *Phys Rev Lett*. 1996;76:624-627.
34. Hartemann FV. *High-Field Electrodynamics*. CRC Press; 2001. Google-Books-ID: 7SDNBQAAQBAJ.
35. Reutershan T, Effarah HH, Barty CPJ. Bayesian optimization of laser-Compton x-ray sources for medical imaging applications. In: *Medical Imaging 2023: Physics of Medical Imaging*. Vol 12463. SPIE; 2023:821-827.
36. Jeukens CRLPN, Lalji UC, Meijer E, et al. Radiation exposure of contrast-enhanced spectral mammography compared with full-field digital mammography. *Invest Radiol*. 2014;49:659.
37. Gennaro G, Cozzi A, Schiaffino S, Sardanelli F, Caumo F. Radiation dose of contrast-enhanced mammography: a two-center prospective comparison. *Cancers*. 2022;14:1774.
38. Konstantinidis AC, Szafraniec MB, Rigon L, et al. X-ray performance evaluation of the Dexela CMOS APS X-ray detector using monochromatic synchrotron radiation in the mammographic energy range. *IEEE Trans Nucl Sci*. 2013;60:3969-3980.
39. Konstantinidis AC, Szafraniec MB, Speller RD, Olivo A. The Dexela 2923 CMOS X-ray detector: a flat panel detector based on CMOS active pixel sensors for medical imaging applications. *Nucl Instrum Methods Phys Res, Sect A*. 2012;689:12-21.
40. Kulpe S, Dierolf M, Günther B, et al. K-edge subtraction computed tomography with a compact synchrotron X-ray source. *Sci Rep*. 2019;9:13332.
41. Boone JM, Seibert JA, Tang C-M, Lane SM. Grid and slot scan scatter reduction in mammography: comparison by using Monte Carlo techniques. *Radiology*. 2002;222:519-527.
42. Jeukens CRLPN. Physics of contrast-enhanced mammography. In: Lobbes M, Jochelson MS, eds. *Contrast-Enhanced Mammography*. Springer International Publishing; 2019:23-39.
43. Tissue substitutes in radiation dosimetry and measurement. Technical Report ICRU-44. International Commission on Radiation Units and Measurements. Bethesda, MD (United States). 1989. ISBN 0913394386.
44. Badano A, Graff CG, Badal A, et al. Evaluation of digital breast tomosynthesis as replacement of full-field digital mammography using an in silico imaging trial. *JAMA Netw Open*. 2018;1:e185474.
45. Yohannes I, Kolditz D, Langner O, Kalender WA. A formulation of tissue- and water-equivalent materials using the stoichiometric analysis method for CT-number calibration in radiotherapy treatment planning. *Phys Med Biol*. 2012;57:1173.
46. Jong RA, Yaffe MJ, Skarpathiotakis M, et al. Contrast-enhanced Digital Mammography: Initial Clinical Experience. *Radiology*. 2003;228:842-850.
47. Perl J, Shin J, Schümann J, Faddegon B, Paganetti H. TOPAS: An innovative proton Monte Carlo platform for research and clinical applications. *Med Phys*. 2012;39:6818-6837.
48. Carrier J-F, Archambault L, Beaulieu L, Roy R. Validation of GEANT4, an object-oriented Monte Carlo toolkit, for simulations in medical physics. *Med Phys*. 2004;31:484-492.
49. Sarno A, Masi M, Antonelli N, et al. Dose volume distribution in digital breast tomosynthesis: a phantom study. *IEEE Trans Radiat Plasma Med Sci*. 2017;1:322-328.
50. di Franco F, Sarno A, Mettivier G, et al. GEANT4 Monte Carlo simulations for virtual clinical trials in breast X-ray imaging: proof of concept. *Physica Med*. 2020;74:133-142.
51. Fedon C, Longo F, Mettivier G, Longo R. GEANT4 for breast dosimetry: parameters optimization study. *Phys Med Biol*. 2015;60:N311.
52. Peli E. Contrast in complex images. *J Opt Soc Am A, JOSAA*. 1990;7:2032-2040.
53. Hunt CH, Hartman RP, Hesley GK. Frequency and severity of adverse effects of iodinated and gadolinium contrast materials: retrospective review of 456,930 doses. *Am J Roentgenol*. 2009;193:1124-1127.
54. Cochran ST, Bomyea K, Sayre JW. Trends in adverse events after IV administration of contrast media. *Am J Roentgenol*. 2001;176:1385-1388.
55. Sarnelli A, Elleaume H, Taibi A, Gambaccini M, Bravin A. K-edge digital subtraction imaging with dichromatic x-ray sources: SNR and dose studies. *Phys Med Biol*. 2006;51:4311.

How to cite this article: Reutershan T, Nguyen CV, Effarah HH, Nelson EC, Chesnut KD, Barty CPJ. Scanning K-edge subtraction (SKES) imaging with laser-compton x-ray sources. *Med Phys*. 2025;1-18.
https://doi.org/10.1002/mp.17638